Weierstraß-Institut
für Angewandte Analysis und Stochastik
Leibniz-Institut im Forschungsverbund Berlin e. V.

Preprint ISSN 2198-5855

Optimal control of semiconductor melts by traveling magnetic fields

Peter Nestler[1], Nico Schlömer[1], Olaf Klein[2], Jürgen Sprekels[2,3], Fredi Tröltzsch[1]

submitted: October 19, 2018

[1] Technische Universität Berlin
Institut für Mathematik
Str. des 17. Juni 136 10623 Berlin
Germany
E-Mail: nestler.peter@googlemail.com
nico.schloemer@gmail.com
troeltzsch@math.tu-berlin.de

[2] Weierstrass Institute
Mohrenstr. 39
10117 Berlin
Germany
E-Mail: olaf.klein@wias-berlin.de
juergen.sprekels@wias-berlin.de

[3] Institut für Mathematik
Humboldt-Universität zu Berlin
Unter den Linden 6
10099 Berlin
Germany

No. +++Preprint-Nummer+++
Berlin 2018

Key words and phrases. Czochralski method, Lorentz force, optimal control, Navier-Stokes equations, heat equation, Maxwell equations.

This work was supported by DFG Research Center MATHEON, "Mathematics for Key Technologies" in Berlin, project C9.

Edited by
Weierstraß-Institut für Angewandte Analysis und Stochastik (WIAS)
Leibniz-Institut im Forschungsverbund Berlin e. V.
Mohrenstraße 39
10117 Berlin
Germany

Fax: +49 30 20372-303
E-Mail: preprint@wias-berlin.de
World Wide Web: http://www.wias-berlin.de/

Optimal control of semiconductor melts by traveling magnetic fields

Peter Nestler, Nico Schlömer[1], Olaf Klein, Jürgen Sprekels, Fredi Tröltzsch[1]

Abstract

In this paper, the optimal control of traveling magnetic fields in a process of crystal growth from the melt of semiconductor materials is considered. As controls, the phase shifts of the voltage in the coils of a heater-magnet module are employed to generate Lorentz forces for stirring the crystal melt in an optimal way. By the use of a new industrial heater-magnet module, the Lorentz forces have a stronger impact on the melt than in earlier technologies. It is known from experiments that during the growth process temperature oscillations with respect to time occur in the neighborhood of the solid-liquid interface. These oscillations may strongly influence the quality of the growing single crystal. As it seems to be impossible to suppress them completely, the main goal of optimization has to be less ambitious, namely, one tries to achieve oscillations that have a small amplitude and a frequency which is sufficiently high such that the solid-liquid interface does not have enough time to react to the oscillations. In our approach, we control the oscillations at a finite number of selected points in the neighborhood of the solidification front. The system dynamics is modeled by a coupled system of partial differential equations that account for instationary heat condution, turbulent melt flow, and magnetic field. We report on numerical methods for solving this system and for the optimization of the whole process. Different objective functionals are tested to reach the goal of optimization.

1 Introduction

1.1 The technology of traveling magnetic fields and the main goal of optimization

The control of the growth of bulk semiconductor (GaAs, Si, Ge) single crystals from the melt by means of traveling magnetic fields has received considerable attention from crystal growing industry worldwide in recent years. The most important industrial technique for the growth of single-crystals from the melt is the so-called “Czochralski method”, depicted in Fig. 1.1. In this configuration, a rotating single crystal seed is dipped into the melt, which is contained in a counter-rotating crucible. The seed is then slowly pulled out of the melt, and a single crystal solidifies.

In the Czochralski process, the melt flow is turbulent, which creates the problem that impurities can find their way into the growing crystal, lowering its quality. Also, crystal growers want the solid-liquid interface (the “free boundary” between melt and crystal) to have a certain shape; moreover, the temperature oscillations of the melt in the region directly below the crystal should have small amplitudes and not too small frequencies, in order that the solidification front has no time to react to them, since this may lead to the growth of crystals of lower quality.

Since the melt is electrically conducting, electromagnetic fields can play the role of a control, since a Lorentz force is induced into the melt in their presence. In the past, time-dependent magnetic fields

DOI 10.20347/WIAS.PREPRINT.+++Preprint-Nummer+++ Berlin 2018

were successfully applied to improve crystal growth processes from the melt. Originally, the magnetic fields were generated by magnets or induction coils placed outside of the growth apparatus. However, with this kind of configuration it requires much energy and some technical efforts to produce a magnetic field of sufficient magnitude in the melt, especially in cases when the thick walls of a pressure chamber shield the magnetic field significantly (e. g., in the growth of III–V compounds with the LEC or VCz processes). In the project KRIST$\widetilde{MAG}^{®}$, an internal heater-magnet module was developed, which consists of several coils that operate as a resistance heater while simultaneously generating a traveling magnetic field. It was demonstrated that this heater-magnet module can produce appropriate magnetic fields in the melt with moderate power consumption (see, e.g., [25, 29, 33, 34]).

In this paper, we aim to demonstrate that – in principle – methods of nonlinear optimization can be applied to achieve the goals mentioned above. Mathematically, one has to solve an optimal control problem for a system of partial differential equations on a complicated, nonsmooth, and axisymmetric domain which is composed of a multitude of subdomains having different material properties. The PDE system features the following components:

– Maxwell's equations for the electromagnetic field,
– a nonlinear heat equation coupled to nonlocal radiation boundary conditions,
– strongly temperature-dependent and anisotropic physical coeffients,
– the Boussinesq approximation of the Navier-Stokes equations for electrically and thermally conducting fluids.

For details of the model, we refer to [6, 9], see also Section 2 below. Fundamental contributions to the mathematical analysis of this model were made in the seminal works [4–9]. The numerical simulation of this highly complex mathematical model was performed for a real growth apparatus in the framework of the project KRIST$\widetilde{MAG}^{®}$ in joint work with the Leibniz Institute for Crystal Growth (IKZ) in Berlin-Adlershof. In this connection, we refer the reader to [24, 25, 26, 29, 33, 34]. Note that the problem studied here is much more involved than that analyzed in [13], where the fluid part was not included.

In this contribution, we show the applicability of mathematical optimization techniques to a simplified model. In particular, we do not consider the transfer of heat from the heater coils to the melt via radiation. Our results show the efficiency of the control by traveling magnetic fields. Although this is done for a simplified setting, the method should be applicable also for the full model. However, the implementation would be essentially more difficult. But already the simplified model is very challenging.

The main goal of the optimization problem posed here is as follows. In a specific spatial point P_1 within the melt (cf. Figure 2.2 for the location of this point), the melt should behave as follows: considered as a function of time, the temperature at P_1 should vary with a sufficiently high frequency, while the amplitudes of the temperature oscillations remain small. We will present a numerical method for the optimization of this process, i.e., for the computation of an optimal traveling magnetic field. To influence the melt flow, traveling magnetic fields are used that are generated by a heater-magnet module, indicated as HMM in Figure 1.1. For controlling purposes, the phase shifts of the voltages in the magnetic induction coils of the HMM are at our disposal. Although the total voltages might be controlled as well, this possibility is not considered in this paper.

The heater-magnet module includes five induction coils that can be separately controlled, i.e., the phase shifts can be fixed for each coil. In this way, our control is just a vector in $\mathbb{R}^5$. We do not consider a time-depending control function as it is often considered in optimal control theory. In this way, the control space is of very low dimension, and we do not have to cope with a control discretization. Instead, the main difficulties originate from other sources. First, the problem is complicated by the curse of dimension, due to the coupled and highly nonlinear system of PDEs that models the behavior of the melt (recall that this system is composed of the nonlinear heat equation for the temperature of

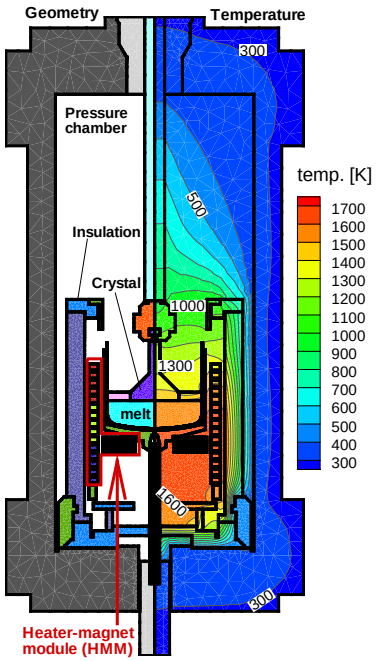

Figure 1.1: Growth apparatus with heater-magnet module and crucible.

the melt, the transient Navier-Stokes equations for the melt flow, and Maxwell type equations for the Lorentz forces); second, the computed fields exhibit a fairly “wild” behavior, close to being chaotic. For this reason, standard methods of optimal control theory such as adjoint-based gradient computations turned out to be useless. While being differentiable in theory (at least in a spatially two-dimensional setting), the control-to-state mapping associating the flow and temperature fields to the control vector turns out to be numerically nondifferentiable. Finding a suitable objective functional that expresses best the aim of our optimization, was another difficult issue. We will report on the application of several functionals that turned out to be useful.

1.2 Related literature

Our paper is a contribution to the field of optimization and control of magneto-hydrodynamical systems (MHD). The numerical analysis of such problems was extensively studied since the mid-nineties of the last century. We refer exemplarily to [22, 23, 20, 21, 17, 36, 15] and the references therein. Moreover, we mention [2, 18, 19]. In [2, 19], the solidification in crystal melts is controlled, while in [18] Lorentz forces are used to control weakly conducting fluids. However, the complexity of these problems is smaller and they are not solved with an industrial background.

In contrast to the abovementioned papers, we discuss a control problem of semiconductor crystal growth having a real industrial background. Moreover, we deal with the optimization of traveling magnetic fields induced by a heater-magnet module located in the interior of the growth apparatus, which is also a new feature. In this technology, the Lorentz forces can have a quite strong influence on the crystal melt.

2 Modeling the system dynamics

The semiconductor melt flow is contained in a crucible, which is the rotationally symmetric three-dimensional bounded domain obtained by rotating the two-dimensional domain of Figure 2.2 about the axis that coincides with its left edge. Throughout this paper, this two-dimensional domain will be denoted by Ω. The crucible, i.e., the three-dimensional domain obtained by rotating Ω, is denoted by Ω. Figure 2.2 also displays the two observation points P_1 and P_2 that we use. In P_1, the optimization criterion of high frequency temperature oscillation with small amplitude is to be met.

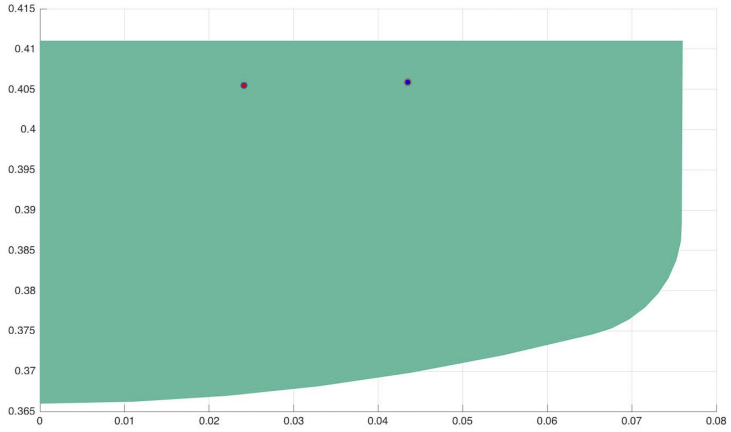

Figure 2.2: Cross section Ω of the crucible with observation points $P_1 = (0.0241, 0.4055)$ (red color, left) and $P_2 = (0.0442, 0.4007)$ (blue color, right); the z-axis is vertical, the r-axis horizontal.

The process is modeled by the evolution equations for the temperature θ, the fluid velocity v, the pressure p, and the Lorentz force f_L, which are discussed next. The model constitutes a simplification of the model considered in, e.g., [6].

2.1 Heat equation

We will frequently use cylindrical coordinates (r, ϕ, z); in particular, for the flow velocity v we have $v = v_r e_r + v_z e_z + v_\phi e_\phi$, where $\{e_r, e_\phi, e_z\}$ is the associated orthogonal system of tangent coordinates. Since we assume that temperature and flow velocity do not depend on the rotation angle ϕ, only the two-dimensional velocity vector $\hat{v} := (v_r, v_z)$ appears in the heat equation. For convenience, we formulate the differential equations in cartesian coordinates. Cylindrical coordinates were used in all computations. Notice that the directions z and r comply with the cartesian coordinates for the two-dimensional domain Ω.

The equations for the heat conduction are

$$\begin{aligned} \rho\, c\,(\partial_t \theta + \hat{v}\cdot\nabla\theta) &= \operatorname{div}(\kappa\nabla\theta) && \text{in } (0,T)\times\Omega, \\ \theta &= g_D && \text{on } \Gamma_D, \\ \kappa\,\partial_n\theta &= g_N && \text{on } \Gamma_N, \\ \partial_n\theta &= 0 && \text{on } \Gamma_0, \\ \theta(0,\cdot) &= \theta_0 && \text{in } \Omega. \end{aligned} \tag{2.1}$$

Here, Γ_D and Γ_N denote the Dirichlet and Neumann boundary parts of the boundary $\partial\Omega$ of the crucible Ω, Γ_0 is the left edge of Ω, i.e., the rotational axis. Γ_0 is part of the Neumann boundary, because there the Neumann data are zero by symmetry. These boundary parts are displayed in Figure 2.3. By ∂_n, we denote the two-dimensional outward normal derivative at the boundary of Ω. By g_D, the given temperature of the melt is denoted, where the solidified semiconductor crystal geometrically "touches" the melt. Observe that we have neglected the heat sources originating from the induction currents within the melt. This seems to be a reasonable simplification, since the Joule heating is likely to be small and of minor importance. To simplify the setting, we further assume that the temperature g_D is constant with respect to time and given. For this purpose, we took a temperature field that was computed by the full model of [24, 26] for the velocity vector $v = 0$, i.e., without convection. A rough description is that g_D and g_N are adapted to the ground temperature for operating the process of crystal growth that was computed by the full model including heat radiation. In Section 3.1, we will report on the concrete selection of g_D, g_N and θ_0.

Numerical implementation

For the numerical solution of the heat equation, we implemented a finite element method with respect to the space variable. Here, triangular finite elements with standard piecewise linear and continuous ansatz functions were applied. Moreover, we used the fractional step scheme with respect to time, see [39, 16]. We also refer to the expositions in [30, 32]. This refined version of the standard Crank-Nicolson method essentially stabilizes the numerical method and yields better results.

2.2 Navier-Stokes equations

The flow of the semiconductor melt was modeled by the three-dimensional instationary Navier-Stokes equations with Boussinesq approximation,

$$\begin{aligned} \rho\,[\partial_t v + (v\cdot\nabla)v] - \nu\Delta v + \nabla p &= f(\theta) + f_L && \text{in } D\times(0,T),\\ \operatorname{div} v &= 0 && \text{in } D\times(0,T),\\ v(\cdot,0) &= v_0(\cdot) && \text{in } D, \end{aligned} \tag{2.2}$$

with density ρ, velocity vector v, pressure p, viscosity ν, bouyancy force $f(\theta)$, and Lorentz force f_L. Here, v_0 is a certain initial flow field that will be specified in Section 3.1. Recall that D is the three-dimensional domain generated by rotating the two-dimensional domain Ω about the z-axis.

Data 1 (Coefficients in heat and Navier-Stokes equations) In the computations, we fixed the density $\rho = 5713\,\frac{kg}{m^3}$, the heat conductivity $\kappa = 17.8\,\frac{W}{mK}$, the heat capacity $c = 434\,\frac{J}{kgK}$, and the viscosity $\nu = 2.8\cdot 10^{-3}$; these data correspond to a GaAs melt.

Boundary conditions

The Navier-Stokes equations have to be complemented by appropriate boundary conditions that depend on the particular parts of the boundary. We formulate them in cylindrical coordinates.

The boundary parts of $\Gamma = \partial\Omega$ are displayed in Figure 2.3. The left edge of Γ, associated with $r = 0$, is denoted by Γ_0. The left upper boundary of the melt surface is depicted in red color. This is

the part $\Gamma_D \subset \Gamma$ where the growing crystal is supposed to touch the melt. The remaining part of Γ, $\Gamma_N = \Gamma \setminus \overline{\Gamma_0 \cup \Gamma_D}$ is the Neumann boundary. The part $\Gamma_S \subset \Gamma_N$ of the Neumann boundary forms the shell of the crucible and $\Gamma_T = \Gamma_N \setminus \overline{\Gamma_S}$ forms the top surface of the melt that is not below the crystal.

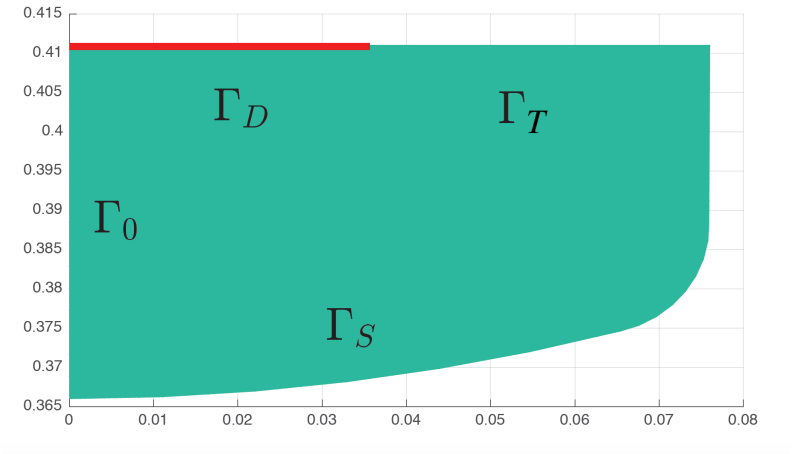

Figure 2.3: Boundary parts of Ω. The Neumann boundary Γ_N is equal to $\Gamma_T \cup \Gamma_S$.

In Γ_0, natural boundary conditions should be satisfied. To improve the stability and convergence properties of the numerical scheme for solving the equations, we fixed the conditions

$$v_r = v_\phi = 0 \text{ on } \Gamma_0.$$

By symmetry, we have natural Neumann boundary data for v_z,

$$\partial_n v_z = 0 \text{ on } \Gamma_0.$$

On Γ_D it is natural to impose a no-slip boundary condition on v_r and to fix $v_z = 0$. Moreover, the growing crystal rotates about the axis $r = 0$ with the constant speed of $-5\,rpm$ (rotations per minute); this is reflected in a Dirichlet boundary condition for v_ϕ on Γ_D,

$$v_r = v_z = 0 \text{ and } v_\phi = -5\,rpm \text{ on } \Gamma_D.$$

The crucible rotates in the opposite direction, so that the no-slip boundary condition on the part of the Neumann boundary forming the shell of the crucible yields that

$$v_r = 0,\, v_z = 0,\, v_\phi = 5\,(rpm) \text{ on } \Gamma_S.$$

On Γ_T, we postulate that the melt cannot move in the direction of the melt surface, leading to a kind of no-slip boundary conditions for v_z. Moreover, we postulate that the surface rotates with the same velocity as the crucible:

$$v_z = 0, v_\phi = 5, \text{ on } \Gamma_T,$$

Summarizing, we use the following boundary conditions for the Navier-Stokes equations:

$$\begin{aligned}
&\text{on } \Gamma_0: \quad v_r = v_\phi = 0,\ \partial_n v_z = 0,\\
&\text{on } \Gamma_D: \quad v_r = v_z = 0, \quad v_\phi = -5,\\
&\text{on } \Gamma_T: \quad v_z = 0, \quad v_\phi = 5,\\
&\text{on } \Gamma_S: \quad v_r = 0, \quad v_z = 0, v_\phi = 5,
\end{aligned} \tag{2.3}$$

Numerical implementation

The rather turbulent behavior of the crystal melt required a very careful selection of the numerical method for the Navier-Stokes equations. As for the heat equation, we applied a fractional step method for the time discretization, [14, 16, 32]. For the space discretization, a finite element method was implemented. Here, we used the (quadratic) Taylor-Hood element along with a grad-div stabilization, see [31]. Moreover, the mass lumping technique [5] was used to avoid the inversion of mass matrices. In view of this, the Taylor-Hood elements were complemented by bubble functions.

Additionally, the Van Kan projection method [38, 16] was implemented. In the implicit convection diffusion step of this method, we resolved the arising linear systems by GMRES. In the pressure correction step, the conjugate gradient method with hierarchical preconditioning was implemented.

2.3 Equations for the magnetic field

The heater-magnet module includes five induction coils that consist of three or four or five windings each. The total number of windings is twenty-two, see Figure 2.4 for the location and main direction of influence of the coils. On the induction coil k, $k \in \{1,\dots,5\}$, the complex voltage $v_k = V_k e^{i\varphi_k}$, is imposed, where $\varphi_k \in [0, 2\pi]$ is the phase shift to be optimized.

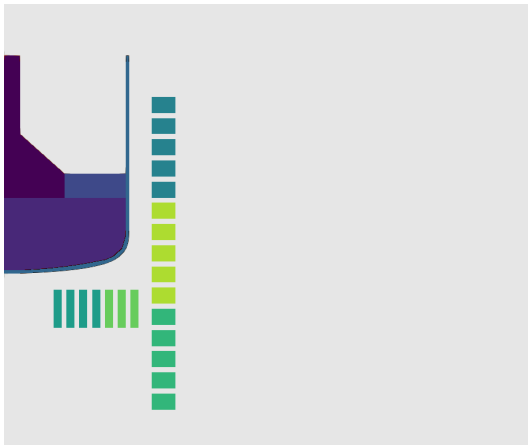

Figure 2.4: Geometry of melting pot and induction coils underlying the numerical tests. From the right lower coil to the very left coil, the number of windings is 5, 5, 5, 3, 4. The distance from the upper boundary of the highest winding to the lower boundary of the lowest one is 0.208 m. The melting pot has a thickness of 3-4 mm. This setting reflects the situation of Fig.1.1; it is also used in the software package *maelstrom*, [37].

The coils in the heater-magnet module (HMM) (heat magnet module) have two aims: first of all, they generate heat by resistive heating within the coils and heat up the growth apparatus and therefore also the crucible and the melt. We do not consider the temperature distribution in the growth apparatus. In our simplified model, the influence of the temperature field in the overall growth apparatus is incorporated via extracting the temperature field in the melt from a simulation of the complete apparatus, generating the ground temperature. This ground temperature is used to generate the the Dirichlet and Neumann boundary data of the heat equation; cf. the remarks in Section 3.1.

The second task of the induction coils, namely the generation of a Lorentz force in the melt by induced magnetic fields, is decisive for the optimization. The Lorentz force f_L depends on the electrical currents in the inductions coils and hence on the vector of phase shifts $\varphi = (\varphi_1,\dots,\varphi_5)$ in the five induction

coils. It is given by

$$f_L(\varphi) = \mathbf{j}(\varphi) \times B(\varphi),$$

where $\mathbf{j} = je_\phi : \mathbf{D} \to \mathbb{C}^3$ denotes the electrical current and $\mathbf{D}$ is a sufficiently large bounded computational domain with smooth boundary that contains D; B stands for the magnetic flux density. In our numerical examples, $\mathbf{D}$ was a ball of radius 1m centered in the middle of the melting pot.

For $B : \mathbf{D} \to \mathbb{C}^3$, we follow the approach in [35] and use the following vector potential ansatz with a complex magnetic potential ψ,

$$B = \mathrm{curl} A, \qquad A = \psi e_\phi .$$

The potential ψ is the solution to an elliptic boundary value problem. To formulate this elliptic problem, let $v_{k\ell}$ and $j_{k\ell}$ denote the total voltage and the electrical current in the winding ℓ of induction coil k, and let n_k be the number of windings of coil k, $k \in \{1,\dots,5\}$, $\ell \in \{1,\dots,n_k\}$. The coils are numbered in the following order: Right lower, right middle, right upper, left coil under the melting pot (4 windings) and right coil under the melting pot (3 windings); cf. Fig. 2.4.

Moreover, let $\Omega_{k\ell}$ denote the cross section of the winding ℓ of coil k, which is orthogonal to the direction of the winding. To find the associated potential ψ, all of the complex-valued voltages $v_{k\ell}$ must be determined. Assume for a while that these voltages are known. Then the scalar complex potential ψ is obtained as the solution to the following elliptic boundary value problem (see [35]):

$$\begin{aligned} -\operatorname{div} \frac{\operatorname{grad}(r\psi)}{\mu\, r} &= \begin{cases} 0 & \text{in the insulators,} \\ -i\omega\sigma\,\psi + \dfrac{\sigma}{2\pi r} v_{k\ell} & \text{in the winding } \ell \text{ of coil } k, \\ -i\omega\sigma\,\psi & \text{in the other conductors,} \end{cases} && \text{in } \mathbf{D} \\ \partial_n \psi &= 0 && \text{on } \partial\mathbf{D}. \end{aligned} \tag{2.4}$$

Here, σ is the electrical conductivity, while μ denotes the magnetic permeability. The boundary value problem (2.4) is complemented by interface conditions on the boundaries between different materials as they are defined in [27]. We should mention that the notation of the potential used in [27] differs from ours. Indeed, the potential ψ used in [27] is related to the potential ψ in (2.4) by $\psi := r\,\psi$, with the potential (2.4) standing on the right-hand side and the one of [27] on the left-hand side.

The electrical current $j_{k\ell}$ in the winding ℓ of coil k is obtained from

$$j_{k\ell} = \frac{v_{k\ell}}{2\pi} \int_{\Omega_{k\ell}} \frac{\sigma}{r}\, dr dz - i\omega \int_{\Omega_{k\ell}} \sigma\,\psi\, dr dz. \tag{2.5}$$

Then the electrical current $j : \mathbf{D} \to \mathbb{C}^3$ is given by

$$j = \begin{cases} 0 & \text{in the nonconducting domain} \\ -i\,\omega\sigma\,\psi + \dfrac{\sigma v_{k\ell}}{2\pi r} & \text{in winding } \ell \text{ of coil } k,\ k \in \{1,\dots,5\},\ \ell \in \{1,\dots,n_k\}, \\ -i\omega\sigma\,\psi & \text{in conductors not being coils (e.g., } D). \end{cases} \tag{2.6}$$

To find the unknown complex-valued voltages $v_{k\ell}$ in the windings, we follow [27]. To this end, we define particular potentials $\psi_{k\ell}$, $k \in \{1,\dots,5\}$, $\ell \in \{1,\dots,n_k\}$, that solve equation (2.4) for the following particular choice of the voltages: for fixed k, ℓ, we solve equation (2.4) with the particular voltages $v_{mn} := u^{kl}_{mn}$, $m \in \{1,\dots,5\}$, $n \in \{1,\dots,n_m\}$, where

$$u^{kl}_{mn} = \begin{cases} 1 & \text{if } m = k,\ n = \ell, \\ 0 & \text{otherwise.} \end{cases} \tag{2.7}$$

Since (2.4) is a linear system, its solution ψ can be obtained by superposition of the particular potentials, i.e.,

$$\psi = \sum_{k=1}^{5} \sum_{\ell=1}^{n_k} v_{k\ell}\, \psi_{k\ell}. \tag{2.8}$$

Now, two additional facts determine the unknown voltages $v_{k\ell}$. First, in all windings of the same coil k, the currents must be the same,

$$j_{k\ell} - j_{k(\ell+1)} = 0, \quad \ell = 1, \ldots, n_k - 1. \tag{2.9}$$

We insert the representation (2.8) for ψ in (2.5). This yields expressions for the $j_{k\ell}$ in terms of the values $v_{k\ell}$. Next, we insert these expressions for the currents $j_{k\ell}$, $j_{\ell(k+1)}$ in (2.9) above. For each coil k, this yields $n_k - 1$ complex homogeneous linear equations for the unknown voltages. The coefficients of the equations can be determined by the integrals in (2.5). In our setting, we have $3 \cdot 4 + 3 + 2 = 17$ such equations.

The second information for fixing the voltages is that

$$\sum_{\ell=1}^{n_k} v_{k\ell} = V_k\, e^{i\varphi_k}, \quad k = 1, \ldots, 5, \tag{2.10}$$

where V_k is the total voltage of the induction coil k.

Data 2 (Voltages) For all the computational examples, we selected the following voltages: $V_1 = V_2 = V_3 = 38\,V$, $V_4 = V_5 = 25\,V$.

In this way, we obtain five additional complex inhomogeneous linear equations. Altogether, we arrive at a linear system

$$A\,w = b \tag{2.11}$$

with a complex 22×22-matrix A and a given complex vector $b \in \mathbb{C}^{22}$ having components that equal either zero or $V_k e^{i\varphi_k}$. The entries of A are easily obtained from (2.8) and the integrals appearing in (2.5). The complex solution vector w contains all unknown voltages $v_{k\ell}$ as components.

Summary for the computation of $f_L(\varphi)$:

Preparatory step: Solve the elliptic equation (2.4) for the 22 particular voltages (2.7), $k = 1, \ldots, 5$, $\ell = 1, \ldots, n_k$, to obtain the particular potentials $\Phi_{k\ell}$. Establish the matrix A as explained above.

Next, the following steps have to be performed:

1 Solve the linear (complex) system of equations $Aw = b$, where – according to our implemented numbering – b has the components

$$b_j = \begin{cases} V_k\, e^{i\varphi_k}, & \text{if } j = 5k \text{ and } k \in \{1,2,3\}, \\ V_4\, e^{i\varphi_4}, & \text{if } j = 19, \\ V_4\, e^{i\varphi_5}, & \text{if } j = 22, \\ 0, & \text{otherwise.} \end{cases}$$

2 Extract the values for $v_{k\ell}$ from w and determine the complex vector potential ψ by superposition,

$$\psi = \sum_{k=1}^{5} \sum_{\ell=1}^{n_k} v_{k\ell} \psi_{k\ell}.$$

3 Compute the electrical current $j = -i\sigma\omega\psi$ in Ω according to (2.6), notice that the induction coils are located outside of Ω.

4 Determine the Lorentz force by

$$f_L = \frac{1}{2}\mathbf{Re}\left(\frac{j}{r}\nabla(r\bar{\psi})\right).$$

Data 3 (Electrical conductivities and magnetic permeabilities) In the magnetic field equations, we fixed the following data: Electrical conductivity σ in $\frac{1}{\Omega m}$: *We took* $\sigma = 0$ *in the argon gas above the melt, in the gas surrounding the crucible, and in the the melting pot. Moreover, we selected* $\sigma = 52000$ *in the induction coils,* $\sigma = 3.0 \cdot 10^{-07}$ *in the solidified GaAs crystal above the melt, cf. [3], and* $\sigma = 7.9 \cdot 10^5$ *in the GaAs melt.* Magnetic permeability in $\frac{H}{m}$: *We computed with* $\mu = \mu_0 := 4\,\pi\,10^{-7}$ *in all materials except the gas surrounding melting pot and induction coils (painted in gray color in Fig. 2.4), where we took* $1.00000037\,\mu_0$. *For the angular frequency, the value* $\omega = 600\,\pi$ *was used.*

Numerical implementation

The Maxwell equations (2.4) were solved using maelstrom [37], a numerical software tool for the solution of magnetohydrodynamics problems in cylindrical coordinates based on FEniCS [1]. A core component of the solver is a preconditioner suggested by Kolmbauer and Langer [28]. Our implementation also followed Chaboudez [4].

3 Optimization of the electromagnetic field

Let us recall the main aim of our optimal control problem, namely to determine phase shifts $\varphi_1, \ldots, \varphi_5$ for the voltages in the five induction coils such that, in the observation point P_1, the temperature θ is oscillating at high frequency and low amplitude with respect to the time. More precisely, the mapping $t \mapsto \theta(P_1, t)$ should exhibit this property.

3.1 Modeling the ground temperature in the crystal melt

As mentioned in the introduction, the full mathematical model of the real crystal growth process is more complex than the simplified one we formulated in the preceding sections. In our model, we assumed that suitable Dirichlet or Neumann boundary data are known for the temperature θ at $\partial\Omega$. In this way, we adopt a heat conduction problem with fixed boundary data. In contrast to this, the full model of [24, 26] includes heat radiation between heater-magnet module HMM and crucible. Moreover, it assumes heat radiation between the free upper surface of the melt and the growth chamber of the furnace. For a precise computation of the temperature and the melt flow, the effects of heat radiation cannot be neglected. However, in our paper we want to address the applicability of optimization methods to the problem posed. We will confirm this for the simplified model only, and it is clear that these methods can be transferred to the full model including heat radiation. This would, however, considerably increase the numerical complexity and the computing time.

The heat in the crystal melt is received from the induction coils of the HMM via radiative heat transfer. In this way, the ground temperature level in the melting pot is generated. In the induction coils, the heat

is generated by resistive heating. After a certain period of time of heating, a sufficiently high ground temperature is achieved.

For the optimization of the process of crystal growth, we assume that the melting pot has already reached the ground temperature. The associated amplitudes V_k of the voltages that account for the heating of the melt are not the subject of optimization. They are kept fixed.

To fix suitable boundary data g_D and g_N in our simplified problem, we took the following approach: associated with given heat generating currents in the heater-magnet module, a temperature field was computed by the full model of [24, 26] including heat radiation but without convection, i.e., we selected the velocity vector $v = 0$ in (2.1). From this temperature field in the domain Ω, we extracted the Neumann and Dirichlet boundary data g_N and g_D that fit best to the pre-computed field. These boundary data are kept fixed during the whole optimization process. In other words, the Dirichlet and Neumann boundary data stand for the boundary data of the ground temperature field without considering the flow of the melt. The distribution of the ground temperature field is shown in Figure 3.1.

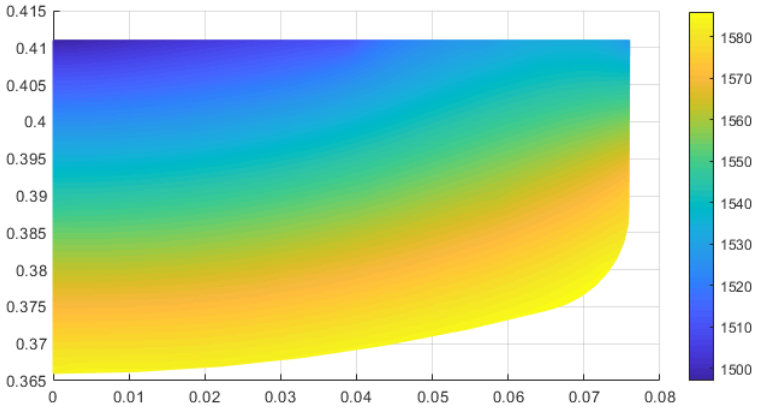

Figure 3.5: Ground temperature of the melt.

3.2 Initial data for the optimization process

In this paragraph, we report on the choice of the initial data θ_0 and v_0 in the equations (2.1) and (2.2).

Initiating from the ground temperature in Figure 3.1, we started our computations without control, i.e., with $f_L = 0$. After a sufficiently long time t_1, the uncontrolled solution exhibits certain basic spatio-temporal patterns that repeat in a fairly stable way, close to being periodic. Let us denote the temperature and velocity fields at t_1 by $\theta_1(x) := \theta(x,t_1)$ and $v_1(x) := v(x,t_1)$, respectively.

While this explains the initial data for the temperature and the flow field equations (2.1) and (2.2), it cannot be recommended to start the mathematical optimization process initiating from these fields $\theta_1(x)$ and $v_1(x)$. This would cause extremely long computing times. Instead, we worked as follows.

Starting with the fields θ_1, v_1 at a new initial time, we imposed a fixed control vector of phase shifts $(\varphi_1^0, \ldots, \varphi_k^0)$ that was known to generate an acceptable behavior of the melt. Associated with that vector, we computed the temperature and flow fields up to the time $t_2 = 300$. The fields $\hat{\theta}_0(x) := \theta(x,t_2)$ and $\hat{v}_0(x) := v(x,t_2)$ were taken as initial data in the equations (2.1) and (2.2). Then the optimization method was applied in the new time period $[0,30]$. The objective functional, however, was evaluated only in $[20,30]$. In other words, the interval of observation is $[20,30]$.

3.3 Objective functionals to be minimized

The main goal of optimization can be achieved in different ways. Let us first report on our attempts to define a suitable objective functional that models this optimization aspect best.

We did not consider problems of vector optimization that would include both aims at the same time (high oscillation and small amplitudes of the temperature in the observation point P_1), since it turned out that the second goal, small amplitudes, was achieved for high temperature frequencies ω_θ automatically. Therefore, we concentrated on maximizing the frequency ω_θ, obtaining small amplitudes as a byproduct. Yet, the aim of maximizing the frequency can be achieved in different ways.

- First, we maximized the number of zeros of the functions $t \mapsto \theta(P_1,t) - \theta_{\min}$ and $t \mapsto \theta(P_1,t) - \theta_{max}$, where $\theta_{\min} < \theta_{\max}$ are suitably chosen real numbers between the observed minimal and maximal values of the real temperature θ. In other words, we counted the number of crossings of the graph of the function $t \mapsto \theta(P_1,t)$ with the lines $\theta = \theta_{\min}$ and $\theta = \theta_{\max}$.

  The maximization of this number of line crossings worked well. Nevertheless, the selection of the values $\theta_{\min}$, $\theta_{\max}$ turned out to be difficult and was not satisfactory.

- We also tried to minimize some first Fourier modes of the function $t \mapsto \theta(P_1,t)$ while some higher Fourier modes were maximized. This criterion was not very successful.

- Finally, we concentrated on maximizing an approximation of the total variation of the function $t \mapsto \theta(P_1,t)$, and on maximizing the L^2-norm of the function $t \mapsto \theta(P_1,t)$. Both these methods were very successful. We will report on this issue in the next paragraphs.

3.3.1 Total variation type functional

We recall that $\varphi = (\varphi_1, \ldots, \varphi_5)$ is the control to be found. As our first favorite objective functional, the following approximation of the total variation of the function $t \mapsto \theta(P_1,t)$ is considered in the fixed time interval $[20,30]$

$$\mathrm{var}(\varphi) := \sum_{i=1}^{\ell} |\theta_\varphi(P_1,t_i) - \theta_\varphi(P_1,t_{i-1})| - \frac{\gamma}{2}|\varphi|^2, \tag{3.12}$$

where $20 = t_0 < t_1 < \ldots < t_\ell = 30$ is an equidistant partition of $[20,30]$ and ℓ was sufficiently large; we took $\ell = 2000$. Here, $|\cdot|$ denotes the Euclidean norm, and $\gamma > 0$ is a small regularization parameter

By the subscript φ as in θ_φ, we indicate that θ_φ is the temperature field associated with the control vector φ of phase shifts. We did not use the functional (3.12) in this form. Instead, we applied the following averaged objective functional J,

$$J(\varphi) := \frac{1}{z(\theta_\varphi)} \sum_{i=1}^{\ell} |\theta_\varphi(P_1,t_i) - \theta_\varphi(P_1,t_{i-1})| - \frac{\gamma}{2}|\varphi|^2, \tag{3.13}$$

where

$$z(\theta_\varphi) = \max \Theta_\varphi - \min \Theta_\varphi \quad \text{and} \quad \Theta_\varphi = \{\theta_\varphi(P_1,t_0), \ldots, \theta_\varphi(P_1,t_n)\}.$$

By averaging with z, the oscillations are better related to the main temperature differences. Associated with the objective functional J, we considered the following optimal control problem (P):

$$\max_{\varphi \in \phi_{ad}} J(\varphi) := \frac{1}{z(\theta_\varphi)} \sum_{i=1}^{\ell} |\theta_\varphi(P_1,t_i) - \theta_\varphi(P_1,t_{i-1})| - \frac{\gamma}{2}|\varphi|^2, \tag{P}$$

subject to the equations

$$\begin{aligned}
\rho\, c\,(\partial_t \theta + v\cdot\nabla\theta) &= \operatorname{div}(\kappa\nabla\theta) \quad \text{in } \Omega\times(0,30),\\
\theta &= g_D \quad \text{on } \Gamma_D,\\
\partial_n\theta &= g_N \quad \text{on } \Gamma_N,\\
\partial_n\theta &= 0 \quad \text{on } \Gamma_0,\\
\theta(0,\cdot) &= \hat{\theta}_0(\cdot),
\end{aligned}$$

$$\begin{aligned}
\rho[\partial_t v + (v\cdot\nabla)v] - \nu\Delta v + \nabla p &= f(\theta) + f_L(\varphi) \quad \text{in } D\times(0,30),\\
v(0,\cdot) &= \hat{v}_0(\cdot),\\
\operatorname{div} v &= 0,
\end{aligned}$$

subject to the boundary conditions (2.3) for the velocity v and

$$F_L(\varphi) = j(\varphi)\times B(\varphi),$$

where $j(\varphi)$ and $B(\varphi)$ are computed as in Section 2.3 and f is the buoyancy force. The set of admissible phase shifts ϕ_{ad} was defined by

$$\phi_{ad} = \{\varphi\in\mathbb{R}^5,\, 0\le\varphi\le 2\pi,\, \varphi_1\ge\varphi_2\ge\varphi_3,\ \varphi_4\le\varphi_5\}.$$

This admissible set includes an important property of the magnetic field that accounts for the Lorentz force: it is chosen as a *traveling magnetic field*.

Remark 1 (i) In the optimization, we fixed the amplitudes V_k in all of the induction coils and optimized only with respect to the phase shifts $\varphi_1,\dots,\varphi_5$. A further optimization of the voltages might be useful as well, but this was not the subject of our investigation and would need some additional constraints.

(ii) The ratio between Lorentz force and buoyancy force is approximately $1:4$. Although the buoyancy force is dominant, the Lorentz force has sufficient influence on the melt.

Remark 2 The function $\varphi\mapsto var(\varphi)$ defines a reduced objective functional, i.e., the state functions θ and v appear only implicitely via the solution of the state equations (2.1), (2.2) and (2.4). To compute J for a given φ, first the Lorentz force $f_L(\varphi)$ is determined by the equations (2.4). Having $f_L(\varphi)$, the coupled system (2.1), (2.2) is solved to obtain θ. Finally, θ is inserted in the functional var to obtain J.

3.3.2 A formula for the frequency

Although the function $t\mapsto\theta(P_1,t)$ exhibits a certain periodic behavior, it is not a periodic function, so that we cannot define a frequency in the standard sense. To have a certain substitute, we invoked a well-known tool of signal processing, the so-called *auto-correlation.* The frequency of a periodic function $y:[-T,T]\to\mathbb{R}$ can be obtained from the auto-correlation function $\tau\mapsto R_y(\tau)$,

$$R_y(\tau) = \int_{-T}^{T} y(t)\,y(t+\tau)\,dt.$$

If y is periodic, then the maximum of R_y is attained at $\tau = 0$, hence by

$$R_y(0) = \int_{-T}^{T} y^2(t)\,dt.$$

For increasing $\tau > 0$, the next local maximum on the right of $\tau = 0$ it attained at $\tau = p(y)$, where $p(y)$ is the period of y. If y is not periodic but behaves like a periodic function, as the function $t \mapsto \theta(P_1,t)$ does, then one can use this information to define a substitute for the frequency. To this end, we consider the auto-correlation function

$$\tau \mapsto R_\theta(\tau) = \int_{-T}^{T} \theta(P_1,t)\cdot\theta(P_1,t+\tau)\,dt$$

and determine its first local maximum on the right of $\tau = 0$. We take the location τ of this local maximum, set $p_\theta := \tau$, and define

$$\omega_\theta := \frac{1}{p_\theta}$$

as a substitute for the frequency the number. On $[-T,0]$, we used the even extension the function $t \mapsto \theta(P_1,t)$. In the numerical tests, the number ω_θ will be indicated to have a quantification for the frequency.

3.4 Numerical examples

3.4.1 Minimization of the total variation functional

All of the optimization runs were started with the initial vector $\varphi^0 = [140, 70,\ 0, 0, 70]$. The objective value for the averaged total variation was $J(\varphi^0) = 2.532186$. The corresponding temperature oscillation in the point P_1 is displayed in Figure 3.6.

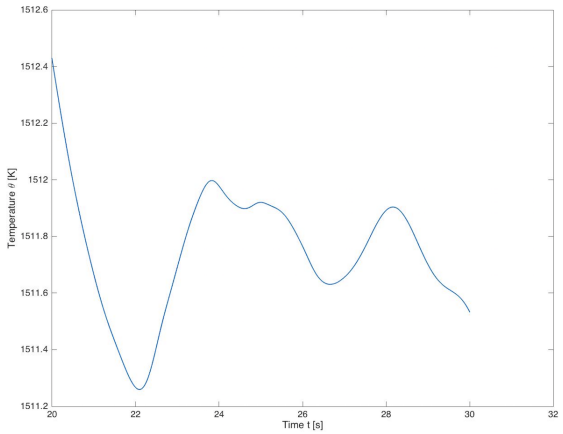

Figure 3.6: Function $t \mapsto \theta(P_1,t)$ for the initial iterate $\varphi^0 = [140, 70, 0, 0, 70]$.

As the numerical optimization method for the total variation functional, we applied the MATLAB code `pattern search` compiled in FORTRAN. We selected this code, since the reduced bounded variation function J is, in principle, numerically not differentiable. Tests with the MATLAB code `fmincon` confirmed that, for our problems, `pattern search` performed better. For the spatial discretization of Ω, we used a fairly coarse grid of about 2000 spatial nodes was used to ensure acceptable running times for the optimization.

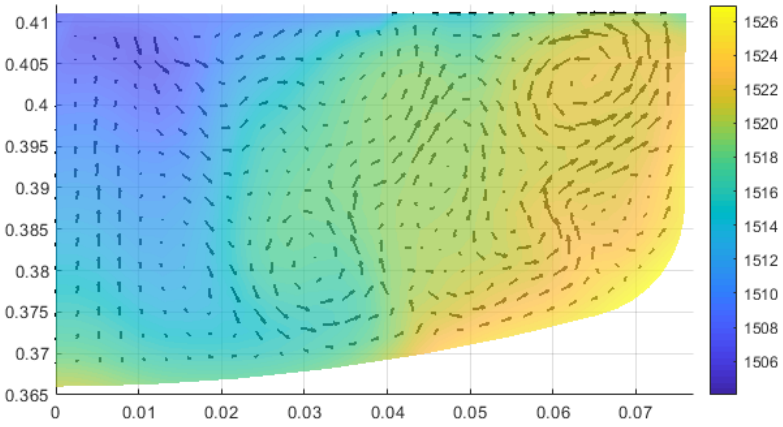

Figure 3.7: Example 1, snapshot of temperature θ and vector field (v_r, v_z) without Lorentz force.

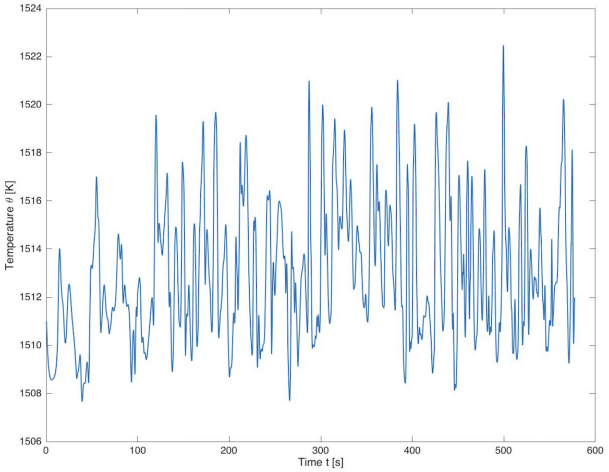

Figure 3.8: Example 1, function $t \mapsto \theta(P_1, t)$ for vanishing Lorentz force.

Example 1 (Solution of the state equations without Lorentz force) To better illustrate the effects of our optimization by Lorentz forces, in Figure 3.7 a snapshot of a typical uncontrolled temperature field θ is displayed along with the associated vector field (v_r, v_z) in the domain Ω. The associated temperature oscillations are shown in Figure 3.8.

Example 2 (Optimization and Crank-Nicolson scheme) In this example, we solved the Navier-Stokes and heat equations using the Crank-Nicolson scheme without fractional-step technique and with the time-step size 0.005. After approximately 200 function evaluations, which needed more than four days on an Intel(R) Core(TM) i7-3720QM CPU @ 2.60GHz with 24.00 GB RAM, the optimization code `pattern search` returned the vector $\varphi = [118, 70, 0.5, 120, 124.5]$; the value of the objective functional is $J(\varphi) = 10.8487$, cf. Fig 3.9 (left). The frequency, determined via auto-correlation, is $\omega_\theta = 0.5362$ Hz. See also Figure 3.9 (right), where the difference between $\tau = 0$ and the location of the next local maximum is approximately $1.865 = 1/0.5362$.

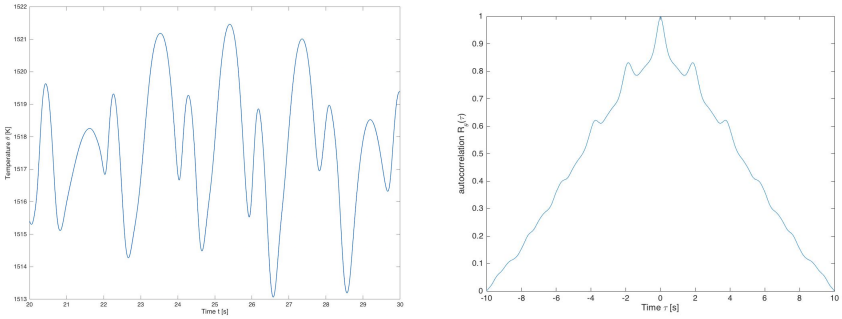

Figure 3.9: Example 2, function $t \mapsto \theta(P_1,t)$ and auto-correlation

Example 3 (Optimization and fractional-step scheme) Here, we improved the stability of the numerical scheme for the state equations using the fractional-step scheme. First of all, the numerical result is more precise. Second, we were able to work with the larger time step 0.01. This reduced the computational time by about two days. The optimal result computed by `pattern search` is $\varphi = [118, 70, 0.5, 120, 124]$ with an associated optimal value $J(\varphi) = 13.8579$, cf. Figure 3.10 (left). The frequency is $\omega_\theta = 0.7576$ Hz; see the auto-correlation plot in Figure 3.10 (right), where the distance between $\tau = 0$ and the next maximum location is close to $1.32 = 1/0.7576$.

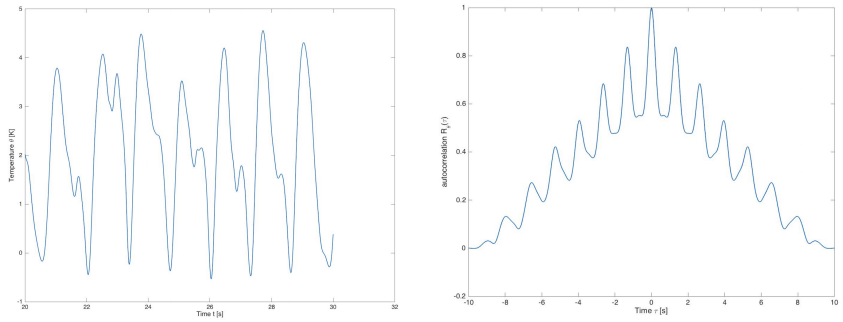

Figure 3.10: Example 3, function $t \mapsto \theta(P_1,t)$ and auto-correlation; in the left figure, the value zero corresponds to a temperature of $1511K$.

3.4.2 Maximization of the energy of $t \mapsto \theta(P_1,t)$

Another useful functional is the L^2-norm of the function $t \mapsto \theta(P_1,t)$, namely

$$J_2(\varphi) := \int_{20}^{30} \theta_\varphi(P_1,t)^2\, dt.$$

Maximizing J_2 subject to the constraints $\varphi \in \Phi_{ad}$ delivered very encouraging results.

Example 4 (Maximization of the L^2-norm) Here, we used the same adjustment as in Example 3, but instead of the total variation functional J, we maximized the energy functional J_2. Now, the objective functional was of integral type and differentiable. Therefore, we invoked the optimization code `fmincon`. The computed optimal shift is $\varphi = [345.40, 139.69, 68.11, 199.45, 199.56]$ with an optimal objective value $J_2(\varphi) = 1.21 \cdot 10^4$ and frequency $\omega_\theta = 0.495$; see Figure 3.11.

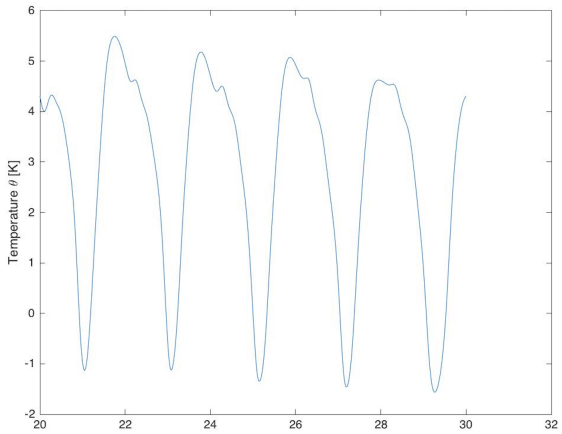

Figure 3.11: Example 4: Function $t \mapsto \theta(P_1, t)$; the value zero corresponds to $1511K$.

References

[1] M. S. Alnæs, J. Blechta, J. Hake, A. Johansson, B. Kehlet, A. Logg, C. Richardson, J. Ring, M. E. Rognes, G. N. Wells, *The FEniCS project version 1.5.*, Archive of Numerical Software **3** (2015).

[2] G. BÄRWOLFF, M. HINZE, *Optimization of semiconductor melts,* Z. Angew. Math. Mech. (ZAMM) **86** (2006), 423–437.

[3] J.S. Blakemore, *Gallium Arsenide: Edited by John S. Blakemore*, Key papers in physics. American Institute of Physics, 1961.

[4] C. Chaboudez, S. Clain, R. Glardon, D. Mari, J. Rappaz, M. Swierkosz, *Numerical modeling in induction heating for axisymmetric geometries,* IEEE Trans. Magn. **33** (1997).

[5] G. COHEN, P. JOLY, J. E. ROBERTS, N. TORDJMAN, *Higher order triangular finite elements with mass lumping for the wave equation*, SIAM J. Numer. Anal. **38** (2001), 2047–2078.

[6] W. DREYER, P.-É. DRUET, O. KLEIN, J. SPREKELS, *Mathematical modeling of Czochralski type growth processes for semiconductor bulk single crystals*, Milan J. Math. **80** (2012), 311–332.

[7] P.-É. DRUET, *Weak solutions to a stationary heat equation with nonlocal radiation boundary condition and right-hand side in L^p*, Math. Meth. Appl. Sci. **32** (2008), 135–166.

[8] P.-É. DRUET, *Existence of weak solutions to the time-dependent MHD equations coupled to the heat equation with nonlocal radiation boundary conditions*, Nonlin. Anal. RWA **10** (2009), 2914–2936.

[9] P.-É. DRUET, *Analysis of a coupled system of partial differential equations modeling the interaction between melt flow, global heat transfer and applied magnetic fields in crystal growth*, Ph.D. Thesis, Humboldt-Universität zu Berlin, 2009.

[10] P.-É. DRUET, *Existence for the stationary MHD-equations coupled to heat transfer with nonlocal radiation effects*, Cz. Math. J. **59** (2009), 791–825.

[11] P.-É. DRUET, *Weak solutions to a model for crystal growth from the melt in changing magnetic fields*, in: “Optimal Control of Coupled Systems of PDE” (K. Kunisch, G. Leugering, J. Sprekels,

F. Tröltzsch, eds.), International Series of Numerical Mathematics **158**, pp. 123–137, Birkhäuser, Basel, 2009.

[12] P.-É. DRUET, *Weak solutions to a time-dependent heat equation with nonlocal radiation boundary condition and arbitrary p-summable right-hand side*, Appl. Math. **55** (2010), 111–149.

[13] P.-É. DRUET, O. KLEIN, J. SPREKELS, F. TRÖLTZSCH, I. YOUSEPT, *Optimal control of three-dimensional state-constrained induction heating problems with nonlocal radiation effects*, SIAM J. Control Optim. **49** (2011), 1707–1736.

[14] J. FROCHTE, *Ein Splitting-Algorithmus höherer Ordnung für die Navier-Stokes-Gleichung auf der Basis der Finite-Element-Methode*, Ph.D. Thesis, University of Duisburg-Essen, 2005.

[15] R. GRIESSE, K. KUNISCH, *Optimal control for a stationary MHD system in velocity-current formulation*, SIAM J. Control Optim. **45** (2006), 1822–1845.

[16] J. L. GUERMOND, P. MINEV, JIE SHEN, *An overview of projection methods for incompressible flows*, Comput. Methods Appl. Mech. Engrg. **195** (2006), 6011–6045.

[17] M. GUNZBURGER, C. TRENCHEA, *Analysis and discretization of an optimal control problem for the time-periodic MHD equations*, J. Math. Anal. Appl. **308** (2005), 440–466.

[18] M. HINZE, *Control of weakly conductive fluids by near wall Lorentz forces*, GAMM-Mitteilungen **30** (2007), 149–158.

[19] M. HINZE, O. PÄTZOLD, S. ZIEGENBALG, *Solidification of a GaAs melt - optimal control of the phase interface*, J. Crystal Growth **311** (2009), 2501–2507.

[20] D. HÖMBERG, J. SOKOŁOWSKI, *Optimal shape design of inductor coils for surface hardening*, Numer. Funct. Anal. Optim. **42**, 1087–1117.

[21] D. HÖMBERG, S. VOLKWEIN, *Control of laser surface hardening by a reduced-order approach using proper orthogonal decomposition*, Mathematical and Computer Modeling **38** (2003), 1003–1028.

[22] L. S. HOU, A. J. MEIR, *Boundary optimal control of MHD flows*, Appl. Math. Optim. **32** (1995), 143–162.

[23] L. S. HOU, S. S. RAVINDRAN, *Computations of boundary optimal control problems for an electrically conducting fluid*, J. Comput. Phys. **128** (1996), 319–330.

[24] O. KLEIN, CH. LECHNER, P.-É DRUET, P. PHILIP, J. SPREKELS, CH. FRANK-ROTSCH, F.-M. KIESSLING, W. MILLER, U. REHSE, P. RUDOLPH, *Numerical simulations of the influence of a traveling magnetic field, generated by an internal heater-magnet module, on Czochralski crystal growth*, in: “Proceedings of the International Scientific Colloquium Modelling for Electromagnetic Processing (MEP2008)” (E. Baacke, B. Nacke, eds.), pp. 91–96. Leibniz University of Hannover, Hannover 2008.

[25] O. KLEIN, CH. LECHNER, P.-É. DRUET, P. PHILIP, J. SPREKELS, CH. FRANK-ROTSCH, F. M. KIESSLING, W. MILLER, U. REHSE, AND P. RUDOLPH, *Numerical simulation of Czochralski crystal growth under the influence of a traveling magnetic field generated by an internal heater-magnet module (HMM)*, J. Crystal Growth **310** (2008), 1523–1532.

[26] O. KLEIN, CH. LECHNER, P.-É DRUET, P. PHILIP, J. SPREKELS, CH. FRANK-ROTSCH, F.-M. KIESSLING, W. MILLER, U. REHSE, P. RUDOLPH, *Numerical simulations of the influence of a traveling magnetic field, generated by an internal heater-magnet module, on liquid encapsulated Czochralski crystal growth*, Magnetohydrodynamics **45** (2009), 557–567.

[27] O. KLEIN, P. PHILIP, *Correct voltage distribution for axisymmetric sinusoidal modeling of induction heating with prescribed current, voltage, or power*, IEEE Trans. Mag., 38, (2002), 1519-ÂĂ-1523.

[28] M. KOLMBAUER AND U. LANGER, *A robust preconditioned MinRes solver for distributed time-periodic eddy current optimal control problems,* SIAM J. Sci. Comput., **34** (2012), B785–B809.

[29] CH. LECHNER, O. KLEIN, P.-É. DRUET, *Development of a software for the numerical simulation of VCz growth under the influence of a traveling magnetic field*, J. Crystal Growth **303** (2007), 161–164.

[30] S. MÜLLER-URBANIAK, *Eine Analyse des Zwischenschritt-θ-Verfahrens zur Lösung der instationären Navier-Stokes-Gleichungen*, Technical Report, Preprint 94-01, SFB 359, University of Heidelberg, 1994.

[31] M. A. OLSHANSKII, A. REUSKEN, *Grad-div stabilization for Stokes equations*, Math. Comp. **73** (2004), 1699–1718.

[32] R. RANNACHER, *Numerische Mathematik 2*, Technical report, University of Heidelberg, 2008.

[33] P. RUDOLPH, *Travelling magnetic fields applied to bulk crystal growth from the melt:The step from basic research to industrial scale*, J. Crystal Growth **310** (2008), 1298–1306.

[34] P. RUDOLPH, CH. FRANK-ROTSCH, F.-M. KIESSLING, W. MILLER, U. REHSE, O. KLEIN, CH. LECHNER, J. SPREKELS, B. NACKE, H. KASJANOV, P. LANGE, M. ZIEM, B. LUX, M. CZUPALLA, O. ROOT, V. TRAUTMANN, G. BETHIN, *Crystal growth in heater-magnet modules – From concept to use*, in: "Proceedings of the International Scientific Colloquium Modelling for Electromagnetic Processing (MEP2008)" (E. Braake, B. Nacke, eds.), pp. 26–29. Leibniz University of Hannover, Hannover 2008.

[35] J. RAPPAZ, M. SWIERKOSZ, *Induction heating for three-dimensional axisymmetric geometries: Modeling and numerical simulation*, in: "Progress in industrial mathematics at ECMI 94", volume **216** of *Lect. Notes in Pure and Appl. Math.*, pp. 317–332. Marcel Dekker, 1995.

[36] S. S. RAVINDRAN, *Real-time computational algorithm for optimal control of an MHD flow system*, SIAM J. Sci. Comput. **26** (2005), 1369–1388 (electronic).

[37] N. SCHLÖMER, *maelstrom: A fast magneto-hydrodynamic FEM solver*, https://github.com/nschloe/maelstrom.

[38] J. VAN KAN, *A second-order accurate pressure-correction scheme for viscous incompressible flow*, SIAM J. Sci. Statist. Comput. **7** (1986), 870–891.

[39] N. N. YANENKO, *The method of fractional steps. The solution of problems of mathematical physics in several variables*, Springer-Verlag, New York-Heidelberg, 1971. Translated from the Russian by T. Cheron. English translation edited by M. Holt.